SCIENCE CHINA
Chemistry

•ARTICLES•

August 2025 Vol.68 No.8: 3844–3851
https://doi.org/10.1007/s11426-024-2516-1

Stepwise activated probe for cell surface glycan imaging

Chunyi Zhang, Jing Chen, Xiaoyao Bai, Shengnan Fu* & Xin Su*

State Key Laboratory of Organic-Inorganic Composites, Beijing Key Laboratory of Bioprocess, Beijing Advanced Innovation Center for Soft Matter Science and Engineering, College of Life Science and Technology, Beijing University of Chemical Technology, Beijing 100029, China

Received November 7, 2024; accepted January 3, 2025; published online February 6, 2025

Fluorescent DNA probes commonly used for *in situ* imaging of cell surface glycans are "always-on" probes (AOPs), which produce high background noise and lack spatial specificity. Molecular dynamics simulations indicate that single-stranded DNA (ssDNA) can stably associate with the cell membrane, contributing to persistent background signals in AOPs. To overcome this challenge, a stepwise activated probe (SAP) is developed for *in situ* imaging of cell surface glycans. In SAP, the cell surface glycan is labeled by rolling circle amplification product through metabolic glycan labeling strategies. The product hybridizes a fluorophore and quencher-labeled ssDNA reporter to form a double strand producing primary enhancement of fluorescence signal. Nicking enzyme (Nb.BbvCI) cleaves the double strand and releases the quencher, further enhancing the signal. Non-specific absorption of the reporter on the cellular membrane does not increase the fluorophore-quencher distance in SAP or trigger Nb.BbvCI cleavage. As a result, only the glycan sites are illuminated. SAP not only exhibits high imaging specificity but also greatly simplifies the imaging procedure by reducing the washing steps. SAP offers a considerable improvement in detection specificity and sensitivity by employing a two-step activation and amplification process, making it a powerful method for *in situ* fluorescence imaging.

***in-situ* glycan imaging, stepwise activated probe, rolling circle amplification, nicking enzyme**

Citation: Zhang C, Chen J, Bai X, Fu S, Su X. Stepwise activated probe for cell surface glycan imaging. *Sci China Chem*, 2025, 68: 3844–3851, https://doi.org/10.1007/s11426-024-2516-1

1 Introduction

Cell surface glycans play crucial roles in cell communication [1,2], disease biomarkers [3,4], immune functions [5–7], and drug targeting and delivery [8,9]. Detecting and imaging cell surface glycans enable the visualization and characterization of specific glycan locations, allowing researchers to uncover molecular interactions and signaling events critical to various biological processes [10–13]. For instance, these methods reveal the spatial distribution of cell surface glycans, providing insights into cellular physiology and disease mechanisms [14–16].

Glycosylation is difficult to directly detect due to its complex conformations and non-template-driven synthesis [17]. Since Bertozzi's group [18] proposed metabolic glycan labeling strategies, these methods have been applied to detect glycosylation in various research targets. Fluorescent DNA probes, known for their excellent versatility and biocompatibility, provide a useful tool for the signal readout of metabolic glycan labeling strategies [19–24]. DNA signal amplification strategies have been developed to enhance signals thereby reducing the use of non-natural sugar labels [25–28]. However, DNA fluorescent probes currently used for cell surface glycan imaging are predominantly "always-on" probes (AOPs). These probes are prone to nonspecific absorption on the cell membrane, leading to high background signals. To mitigate the nonspecific absorption of AOPs, tedious washing steps are required during cell imaging [29]. This process is inefficient, labor-intensive, time-consuming, and negatively affects cell viability. Additionally, such

*Corresponding authors (email: fushengnan317@163.com; xinsu@mail.buct.edu.cn)

washing steps increase the risk of losing signals from highly expressed glycans, substantially reducing imaging accuracy. Therefore, it is motivated to develop a more efficient strategy to overcome the limitations of current fluorescent DNA probes.

Herein, we developed a stepwise activated probe (SAP) to improve the specificity and accuracy of *in situ* imaging of cell membrane glycans. As shown in Figure 1, azide molecules are first incorporated into glycans on the cell surface through metabolic processes. Next, rolling circle amplification (RCA) primers are linked to the glycans via a bioorthogonal reaction. RCA is then initiated, producing long single-stranded DNA (ssDNA) with repeated sequences. A fluorophore-labeled and quencher-labeled reporter ssDNA then hybridizes with the RCA product, leading to primary signal enhancement due to the extended separation between the fluorophore and quencher. When the nicking enzyme, Nb.BbvCI, cleaves the complex, the quencher is released, further boosting the signal. Importantly, nonspecific absorption of the reporter on the cellular membrane does not increase the fluorophore-quencher distance or trigger Nb.BbvCI cleavage. As a result, only the glycan sites are illuminated. SAP not only exhibits high imaging specificity but also greatly simplifies the imaging procedure by reducing the washing steps. In contrast, nonspecific absorption of AOPs leads to high background and false spatial signals. Molecular dynamics (MD) simulations indicated that interactions between the ssDNA backbone and membrane phospholipids cause ssDNA to attach to the cell membrane, explaining the high background signals. We successfully utilized SAP to track changes in cell surface glycans. Compared to traditional AOPs, SAP provides a more reliable method for *in situ* fluorescence imaging of cell surface glycans, potentially advancing research on glycan roles in disease progression and therapeutic interventions.

2 Experimental

2.1 Simulation of ssDNA immobilization on the mammalian cell membrane

Molecular simulation experiments were executed using molecular operating environment (MOE)-Dock from the Chemical Computing Group Inc. The ssDNA model was constructed first. The three-dimensional (3D) model of ssDNA was constructed by following the pipeline established by our group, using DNAfold, RNAComposer, and X3DNA webservers. The 3D coordinates of the ssDNA model were rebuilt to fix missing atoms using the MDWeb version 1.0 web server, which employed the AMBERTools version 1.2 engine. Following this, a mammalian cell membrane model was constructed. The molecular model of the mammalian cell membrane containing 100 molecules of lipids on each face was prepared using the CHARMM-GUI membrane builder module. The built structure was visualized and prepared for docking by the UCSF Chimera program. Both 3D structures of ssDNA and membrane were imported into MOE, and hydrogen atoms were added to the structure with their standard geometry followed by their energy minimization using MOPAC 7.0. A regular procedure of mole-

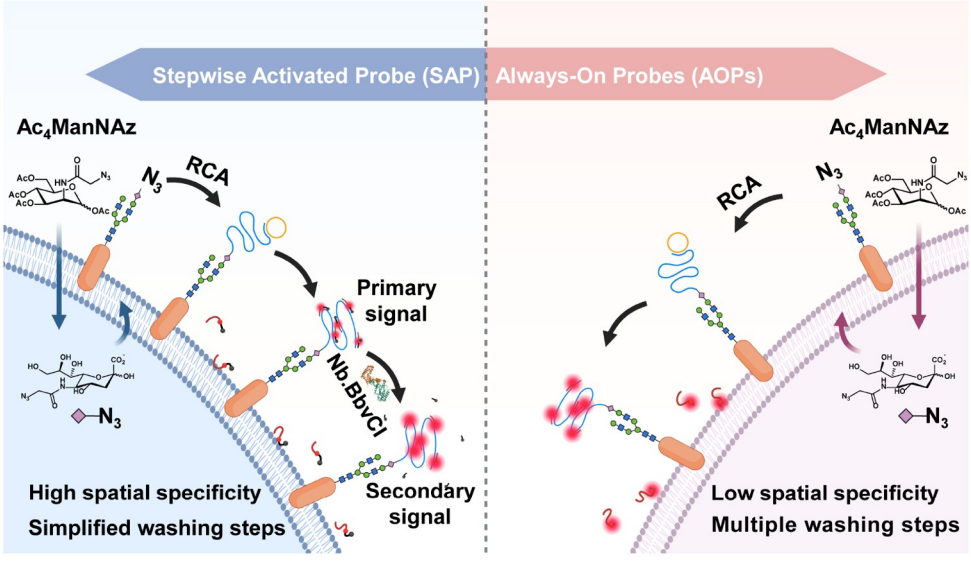

Figure 1 (Color online) Schematic of SAP and AOPs for imaging of cell surface glycan. Azido groups are introduced into cells through metabolic labeling. RCA primers are attached to the glycan sites via a bioorthogonal reaction, initiating an RCA reaction that synthesizes long ssDNA. In SAP, the fluorophore-labeled and quencher-labeled reporter does not emit any signal initially but generates the primary signal upon binding with the RCA product. After hydrolysis by the Nb.BbvCI, a secondary signal is produced. In contrast, AOPs result in false spatial signals because the fluorescent ssDNA binds simultaneously to both the RCA product and the cell membrane.

cular docking was utilized. The lowest energy-minimized pose was used for calculating the energy parameters via AMBER99 force field energy calculation and predicting the docked interactions at the surface of the membrane with ssDNA. Manual screening was performed, and the top 100 docking poses were clustered for the top 3 docking poses with a similar binding site and lowest binding free energy.

In addition, the MD simulation study was carried out for the ssDNA-membrane complex (pose 1) using the standard default parameter setting in the MOE software. MOE software includes four algorithms for MD simulations. In this study, the Nosé-Poincaré-Andesen (NPA), the most precise and sensitive algorithm, was used to study the MD of the ssDNA-membrane complex. In MD calculations, AMBER99 force field, sphere shape, water as a solvent, six margins, and delete far existing solvent with a distance greater than 4 Å were selected to optimize the system.

2.2 Preparation and characterization of SAP

First, primer (final concentration of 200 nM), padlock (200 nM) and T4 DNA ligase (100 U/mL) were mixed in 1× T4 DNA ligase reaction buffer, and the mixture was incubated at 22 °C for 1 h to form a circular product. Then, the solution was mixed with deoxy-ribonucleoside triphosphate (dNTP) (2 mM) and phi29 DNA polymerase (2.0 U/mL) in 1× phi29 DNA polymerase reaction buffer. The mixture was incubated at 37 °C for 1 h for RCA. Finally, for the nicking enzyme cleavage, the solution and T strand (final concentration of 1 μM) were mixed in 1× rCutSmart buffer. Nb.BbvCI was then added to a final concentration of 500 U/mL, and the mixture was incubated at 37 °C for 1 h. To verify the formation of circular padlock DNA, Exonuclease III was added to the ligated product and incubated at 37 °C for 1 h. Characterization of each step in the preparation was performed by native polyacrylamide gel electrophoresis (PAGE, 120 V, 70 min) in 1× TBE-Mg^{2+} buffer (90 mM Tris, 90 mM boric acid, 2 mM EDTA-Na2, and 12.5 mM $MgCl_2$, pH 8) at 4 °C. The gel was then stained by SYBR™ Gold in 0.5× TBE buffer for 30 min and imaged using a gel imaging system (Tanon, China).

2.3 oxDNA simulation of SAP

The SAP structure was simulated using oxDNA molecular simulation software. DNA structures under various conditions were created and edited using oxView website. The simulation parameters, such as time interval, simulation steps, and temperature are detailed in Table S2 Supporting Information online. Virtual Move Monte Carlo (VMMC) algorithm was used to model the spatial distance changes between the bases of Cy5 and BHQ3 in the simulation. A total of 100000 simulation steps were taken, and 1000 data points were extracted from respective trajectories. Finally, python scripts in oxDNA_analysis_tools were used to analyze the data.

2.4 Monitoring of SAP signal generation by fluorescence

The fluorescence assay of SAP was performed *in vitro*. In general, all reactions were completed in 20 μL solutions. Once the reaction was started, it was immediately placed in a real-time polymerase chain reaction (PCR) cycler (Rotor Gene Q, QIAGEN, Germany) to capture the fluorescence signal. Cy5 channel (ex: 650 nm, em: 670 nm) was monitored at 37 °C for 5 s/cycle.

2.5 Operating SAP for imaging targets on polystyrene beads

To operate SAP on polystyrene beads, a 20 μL solution containing 100 nM padlock, 10 nM biotin-Primer, 100 U/mL of T4 DNA ligase and 1× T4 DNA ligase reaction buffer was firstly incubated at 22 °C for 1 h. Subsequently, the above solution was added to 2 mM dNTP, 2.0 U/mL of phi29 DNA polymerase, 1× phi29 DNA polymerase reaction buffer and 10 nM polystyrene beads to 50 μL and incubated for 1 h at 37 °C. At the end of the incubation, 25 μL of the solution was taken to make 50 μL of a solution containing 1× rCutSmart buffer, 1 μM reporter, and 500 U/mL Nb.BbvCI, and incubated at 37 °C for 1 h. Then the solution was placed in a confocal dish and diluted to 200 μL. Fluorescence images of polystyrene beads were obtained by highly inclined laminated optical sheet (HILO) fluorescence microscopy. HILO fluorescence microscope was constructed using a Nikon inverted microscope (ECLIPSE Ti-U, Nikon, Japan) equipped with a 100× magnification, 1.49 numerical aperture (NA) total internal reflection fluorescent microscope (TIRFM) objective (Nikon, Japan) and an electron multiplying charge coupled device (EMCCD) camera (iXon 897, Andor, UK). A 670 nm optical filter (Semrock, USA) was used to detect Cy5 fluorescence (ex: 650 nm, em: 670 nm).

2.6 Metabolic labeling and imaging on cell surface using SAP

A549 cells were cultured in RPMI 1640 medium with 10% fetal bovine serum (FBS) and 1% penicillin-streptomycin solution at 37 °C in a humidified incubator containing 5% CO_2 by volume. For metabolic labeling, Ac_4ManNAz was dissolved in dimethylsulfoxide (DMSO) as a stock solution. Then, cells were seeded at a concentration of 1.5×10^5 cells/mL in the medium and treated with 15 μM Ac_4ManNAz for 48 h. The cells were washed twice with phosphate buffer saline (PBS) after being successfully labeled with azide. For

the bioorthogonal reaction, cells were incubated with 100 μL of a solution containing 1 nM dibenzocyclooctyne (DBCO)-Primer and 1× PBS for 1 h at 22 °C. Next, cells were incubated with 10 nM padlock, 100 U/mL T4 DNA ligase and 1× T4 DNA ligase reaction buffer for 1 h at 22 °C, after which the solution was discarded. Subsequently, cells were incubated with 2 mM dNTP, 2.0 U/mL phi29 DNA polymerase, 1× phi29 DNA polymerase buffer and incubated for 1 h at 37 °C for RCA. Finally, cells were incubated with 1 μM reporter, 500 U/mL Nb.BbvCI, 1× rCutSmart buffer and 5 μg/mL of Hoechst 33342 staining solution at 37 °C for 1 h. Following the above-mentioned step, the cell surface was imaged using an HILO fluorescence microscope. Hoechst 33342 (ex: 350 nm, em:460 nm) was used to stain the nucleus.

For drug treatment, A549 cells were cultured with a mixture of 15 μM Ac_4ManNAz and tunicamycin (TM) at varying concentrations (0, 12.5, 20, 25, and 50 ng/mL) in the previously mentioned medium for 48 h. The cell surface imaging steps were then followed as previously described.

3 Results and discussion

3.1 Study of ssDNA absorption on the mammalian cell membrane surface by molecular docking

The key issue hindering the imaging performance of cell surface glycans is high background noise, primarily due to strong nonspecific adsorption of fluorescent probes [30]. AOPs can lead to high background signals and continuous emission during detection processes [29,31]. To investigate the underlying causes of this phenomenon, we employed molecular simulations to elucidate the mechanism of ssDNA absorption on the cell membrane. The binding free energy ΔG between the cell membrane and ssDNA represented the adsorption stability. Top three poses were shown, yielding ΔG values of −19.56, −17.39 and −16.84 kcal/mol, respectively (Figure 2a). Interestingly, all three poses exhibited prominent changes in the secondary structure of ssDNA upon approaching the membrane surface, indicating increased affinity. This phenomenon was attributed to the necessity for ssDNA to alter its conformation to establish a stable complex, which was further elucidated through MD simulations.

The native ssDNA predominantly displayed a random coil conformation. Significant conformational changes were observed in all three primary poses upon binding with the mammalian membrane surface. MD simulations were run for 200 ns to evaluate the binding dynamics of ssDNA to the membrane surface. Six key points were identified on the root mean square deviation (RMSD) graph, each corresponding to distinct stages of conformational changes (Figure 2b). Analysis of the ssDNA structures at these six points revealed

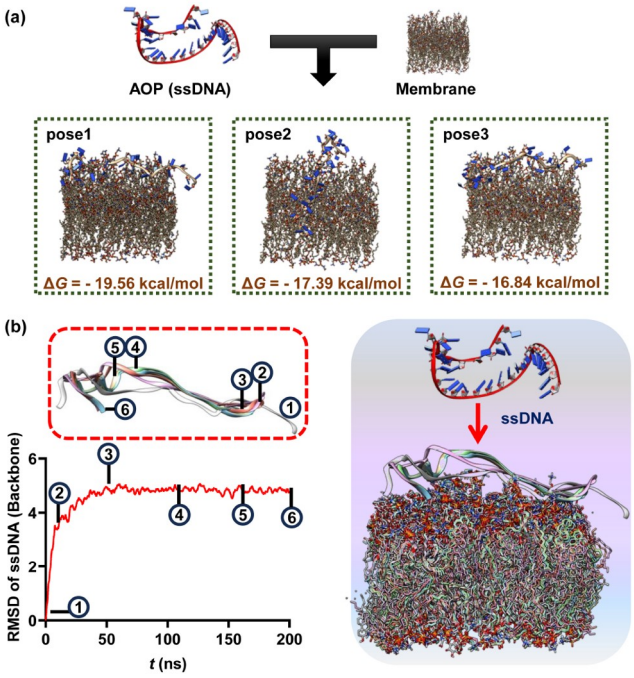

Figure 2 (Color online) Simulation of ssDNA (AOP) absorption on the cell membrane. (a) Visualization of ssDNA absorption onto cell membrane through molecular docking analysis, showing the absorption poses of ssDNA onto the surface of a cell membrane. (b) MD simulations show the interactions between the ssDNA backbone and membrane phospholipids cause ssDNA to attach to the cell membrane. MD simulations were conducted over a duration of 200 ns to explore the behavior of the ssDNA-membrane complex. The RMSD of the ssDNA backbone provides insights into the progressive alterations in conformation.

the dynamic adjustments occurring in the backbone, primarily determined by interactions with the positively charged heads of various phospholipids present on the cell membrane. These interactions induced a series of conformational changes within the ssDNA structure. These findings suggest that the interactions between the ssDNA backbone and phospholipids cause ssDNA to attach to the cell membrane, explaining the continuous background signals in AOPs. As expected, DNA reporter labeled with Cy5 results in background fluorescence (Figure S1 Supporting Information online). In contrast, the reporter modified with both Cy5 and BHQ3 on the cell membrane generates weak background noise (Figure S2).

3.2 Principle and characterization of SAP reactions

We designed SAP for accurately reporting the spatial sites of glycans by generating primary and secondary signals (Figure 3a). RCA is extensively utilized in detection and imaging due to its highly efficient *in situ* signal amplification capability [26,32–34]. Nb.BbvCI exhibits high specificity and sensitivity, as confirmed by fluorescence kinetic experiments (Figure S3). It can be employed in conjunction with a variety of DNA probes and amplification methodologies to accom-

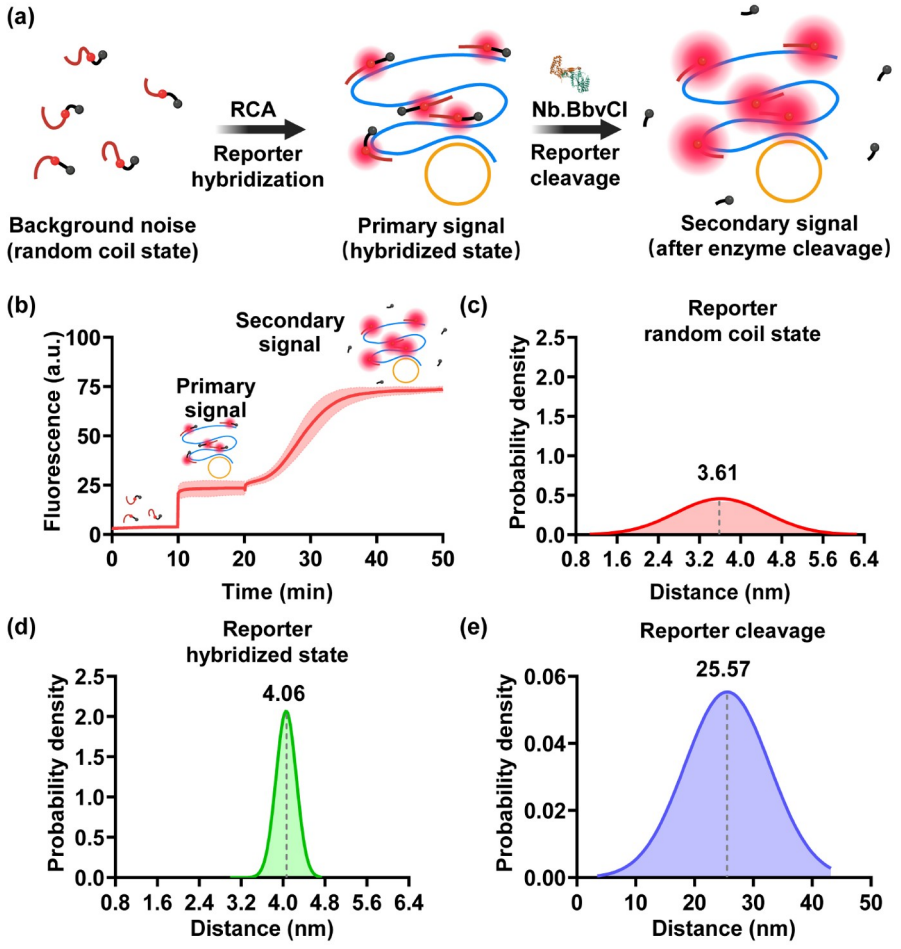

Figure 3 (Color online) Validation and simulation of SAP's signal generation. (a) Schematic of the two-step signal activation for SAP *in vitro*. (b) Fluorescence kinetics of SAP two-step signal activation. (c–e) The distance distribution of fluorophore and quencher in the three states of the SAP reporter: random coil state (c), hybridized state (d) and the state after enzyme cleavage (e).

modate diverse detection requirements [35–37].

SAP was designed including RCA and Nb.BbvCI enzymatic reactions. First, a fluorophore-labeled and quencher-labeled reporter ssDNA hybridizes with the RCA product, leading to primary signal enhancement due to the extended separation between the fluorophore and quencher. Then Nb.BbvCI cleaves the complex, and the quencher is released leading to the secondary signal enhancement (Figure 3a). The stepwise fluorescence signal of SAP is shown in Figure 3b. The primary signal was 5.6-fold higher than background noise and the secondary signal was 4.4-fold higher than the primary signal. Furthermore, we verified the fluorescence kinetics of SAP in a homogeneous solution containing 10% FBS, which demonstrated the stability and specificity of SAP in complex biological environments (Figure S4). Optimization of SAP was performed to maximize fluorescence intensity. Results showed that using 0.1 U/mL of phi29 DNA polymerase (Figure S5), an incubation time of 60 min (Figure S6), and 500 U/mL of Nb.BbvCI (Figure S7) provided the optimal conditions for SAP. Owing to the characteristics of reporter hybridization and enzyme cleavage, only the reporters on the target site (RCA products) can be activated guaranteeing the spatial specificity for *in situ* imaging. We further utilized PAGE to validate the products of Nb.BbvCI enzymatic reactions (lanes 1 and 2, Figure S8), RCA (lanes 1–5, Figure S9), and SAP (lane 7, Figure S9).

To further study the principle of two-step signal generation for SAP, the distances between bases modified with BHQ3 and Cy5 on the reporter were calculated using MD simulations. SAP's two-step activation signal corresponds to the reporter's three states: the random coil state (background noise), the hybridized state (primary signal), and the state after enzyme cleavage (secondary signal). The probability density functions of these distances were calculated. For random coil state, the distance distribution between BHQ3 and Cy5 was broad with an average distance of 3.61 nm (Figure 3c). After hybridization, the distance probability distribution was narrower, and the average distance increased to 4.06 nm (Figure 3d), thus resulting in the activa-

tion of the primary signal. The root mean square fluctuation (RMSF) was used to analyze the DNA structure and evaluate its dynamic stability [38,39]. The median RMSF for the random coil state (RMSF=0.96 nm) was approximately 2.67-fold higher than that for the hybridized state (RMSF= 0.36 nm) (Figure S10), indicating higher reporter stability and explaining the narrower distance probability distribution in the hybridized state. After enzyme cleavage, BHQ3 and Cy5 were separated, and their average distance increased to 25.57 nm, thus resulting in the activation of the secondary signal (Figure 3e). The simulation of the distance changes between BHQ3 and Cy5 on the reporter theoretically demonstrates that SAP can achieve stepwise signal activation, which agrees with the experimental findings.

3.3 Operating SAP for imaging targets on polystyrene beads

To demonstrate the ability of SAP to detect targets on particle surfaces, we first used polystyrene beads instead of cells for fluorescence imaging. The beads are commonly utilized in analytical applications due to their large surface area and strong adsorption properties, making them an ideal platform for the validation of SAP imaging [40].

The modified streptavidin on the bead surface interacts with the biotin attached to the 5′ end of the RCA primer, enabling the anchoring of SAP to beads (Figure 4a). When the RCA primer was not biotinylated, the reporter could not be loaded onto the beads, resulting in a weak fluorescence signal on the bead surface (Figure 4b). When the RCA product hybridized with the reporter carrying Cy5 and BHQ3, a primary signal enhancement occurred due to the extended separation between Cy5 and BHQ3. Subsequently, when Nb.BbvCI cleaved the complex, the quencher was released, further boosting the signal. The primary and secondary signals were found to be 2-fold and 3-fold higher, respectively, than the background signal (Figure 4c). These results demonstrate that SAP can achieve stepwise signal enhancement on target site of polystyrene beads and pave the way for SAP for *in situ* imaging of cell surface glycans.

3.4 Using SAP for imaging cell surface glycan

Metabolic glycan labeling strategies have been widely used to detect glycosylation on cell surfaces. Ac_4ManNAz is one of the most common azide sugars used for metabolic glycan labeling [41–43]. In this study, human non-small cell lung cancer A549 cells were pretreated with Ac_4ManNAz (Ac_4ManNAz (+)) for 48 h, and cells were washed. Then, DBCO-primer was introduced and linked to the cell surface

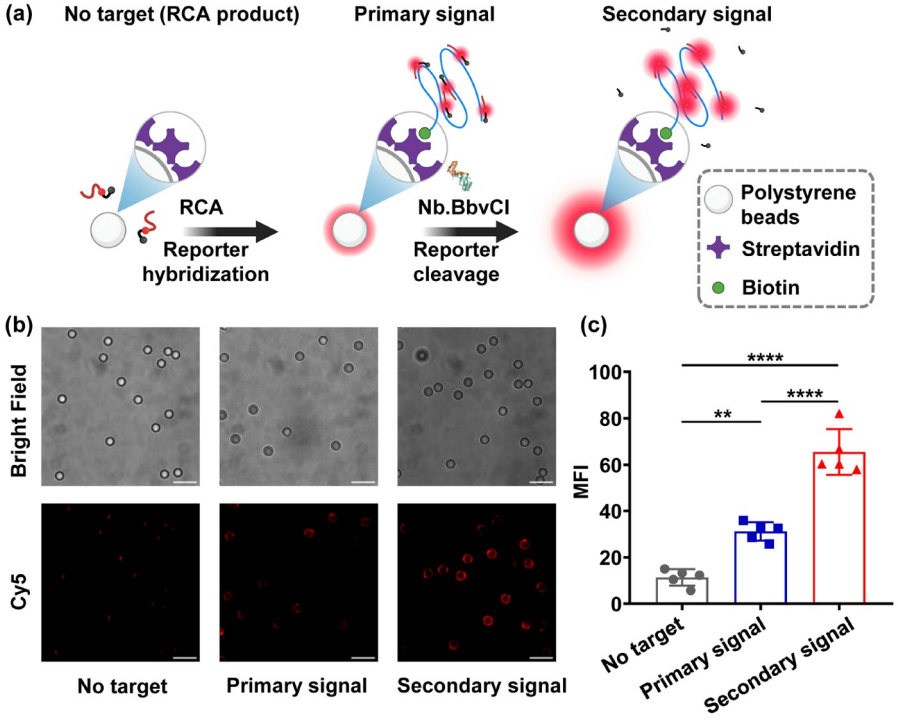

Figure 4 (Color online) SAP for imaging target on polystyrene beads. (a) Schematic of SAP imaging on polystyrene beads. A primary signal is generated when the reporter binds to the RCA product, followed by a secondary, stronger fluorescence signal that is produced upon cleavage of the reporter by Nb.BbvCI. Fluorescence images (b) and mean fluorescence intensities (c) of SAP on the surface of the beads. The concentrations of biotin-primer, padlock, T4 DNA ligase, phi29 DNA polymerase, Nb.BbvCI, and reporter were 10 nM, 100 nM, 100 U/mL, 2.0 U/mL, 500 U/mL, and 1 μM, respectively. Scale bar: 5 μm. Data are presented as means ± s.d. ($n = 5$ independent experiments, 4 field-of-view analyzed in each replicate). Statistical significance was determined by unpaired *t*-tests. $^{**}P < 0.01$, $^{****}P < 0.0001$.

glycans through a bioorthogonal chemistry reaction (Figure 5a). Following the addition of T4 DNA ligase and phi29 DNA polymerase, RCA was initiated, producing long ssDNA with repeated sequences. The reporter hybridized with the RCA product, leading to primary signal enhancement due to the extended separation between the fluorophore and quencher (Figure 5b(i)). Upon cleavage by Nb.BbvCI, the quencher was released, resulting in further signal enhancement (Figure 5b(ii)). Importantly, only the glycan sites are illuminated, as no fluorescence signal was detected on the surfaces of cells that were not pretreated with Ac_4ManNAz (Ac_4ManNAz (−)) (Figure 5b(iii)). Statistically significant differences in fluorescence intensity were observed between Ac_4ManNAz (−) and Ac_4ManNAz (+). The primary and secondary signals for Ac_4ManNAz (+) were 2.2-fold and 3.2-fold higher than the signal for the Ac_4ManNAz (−), respectively (Figure 5b). Owing to the high specificity of SAP, only the glycan sites are illuminated. In contrast, AOPs generated almost indistinguishable signals for Ac_4ManNAz (+) and Ac_4ManNAz (−) (Figure 5c). These results are consistent with the findings of MD simulations of AOP (Figure 2). We also stained the cellular membrane of the Ac_4ManNAz (+) group with wheat germ agglutinin (WGA) to colocalize with the glycan fluorescence signal (Figure S11). This colocalization analysis showed a Pearson correlation coefficient of 0.56 [44]. Collectively, SAP not only exhibits high imaging specificity but also greatly simplifies the imaging procedure by reducing the washing steps.

To validate the ability of SAP to detect glycosylation changes on cell membranes, TM was used to inhibit *N*-glycosylation on A549 cell membranes in a concentration-dependent manner [45–47]. A549 cells were treated with different TM concentrations (0, 12.5, 20, 25, and 50 ng/mL). As the concentration of TM increased, the fluorescence signal observed on the A549 cell membranes gradually decreased (Figure S12a). The signal was reduced to 40% after

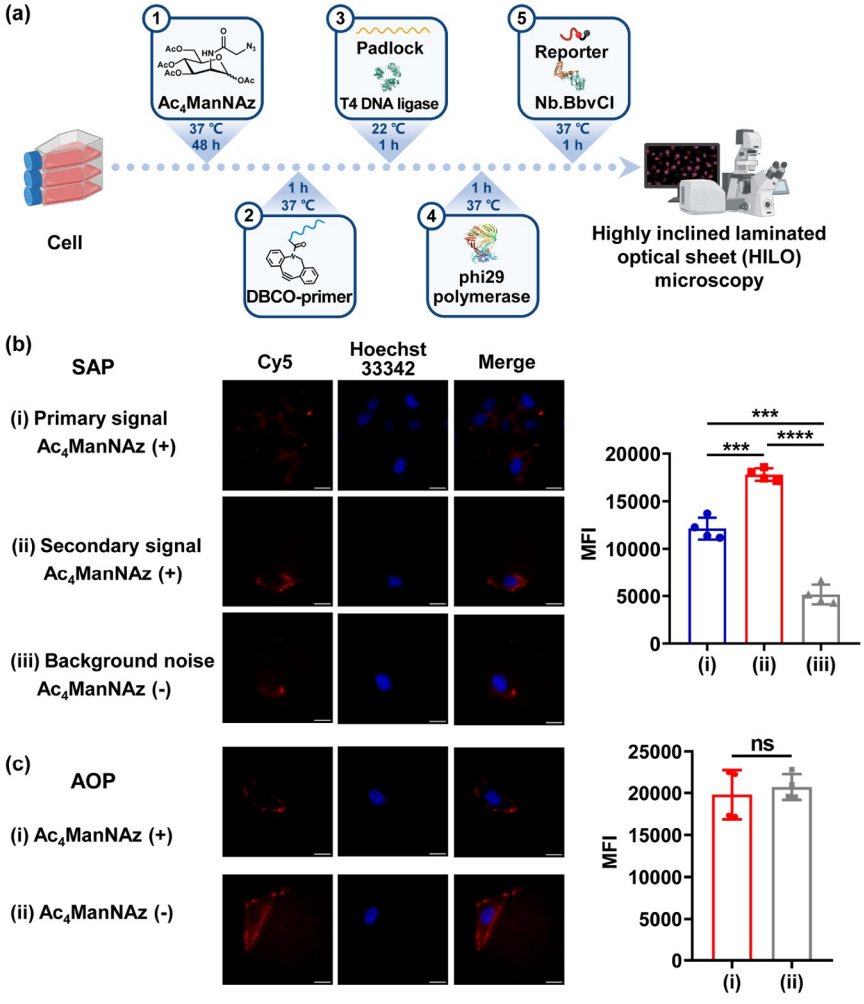

Figure 5 (Color online) *In situ* glycan imaging using SAP on A549 cell surface. (a) The flowchart of cell surface glycans imaging using SAP. Fluorescence images and mean fluorescence intensity of SAP (b) and AOPs (c) on the surface of A549 cells. The concentrations of DBCO-primer, padlock, T4 DNA ligase, phi29 DNA polymerase, Nb.BbvCI, and reporter were 1 nM, 10 nM, 100 U/mL, 2.0 U/mL, 500 U/mL, and 1 μM, respectively. Scale bar: 5 μm. Data are the means ± s.d. ($n = 4$ independent experiments, 4 field-of-view analyzed in each replicate). Statistical significance was determined by unpaired *t*-tests. ***$P < 0.001$, ****$P < 0.0001$.

the treatment with 50 ng/mL of TM (Figure S12b). These results indicate that SAP can monitor cell-surface glycosylation changes during drug treatment and possesses great potential for research on the glycosylation mechanism.

4 Conclusions

In summary, a stepwise activated DNA probe has been developed for *in situ* imaging of cell surface glycans. This probe employs a two-step signal activation process, involving reporter hybridization and cleavage, to enhance both the sensitivity and specificity of cell surface glycan detection. Additionally, it simplifies the imaging procedure by reducing the washing steps, offering a substantial improvement over AOPs. The nonspecific absorption of AOPs on cell membranes results in high background noise, necessitating washing steps to reduce these signals. SAP's high sensitivity and specificity, coupled with its streamlined imaging process, enhance its clinical application potential and are significantly important for early disease diagnosis, prognosis, and therapeutic monitoring.

Acknowledgements This work was supported by the National Natural Science Foundation of China (32271521, 31971361, and 82170763), the State Key Research Development Program of China (2022YFC2603902), the Natural Science Foundation of Beijing Municipality (5212013), the Fundamental Research Funds for the Central Universities (PT2406), and the Talent Cultivation of State Key Laboratory of Organic–Inorganic Composites, Beijing University of Chemical Technology (oic-2024020007).

Conflict of interest The authors declare no conflict of interest.

Supporting information The supporting information is available online at http://chem.scichina.com and http://link.springer.com/journal/11426. The supporting materials are published as submitted, without typesetting or editing. The responsibility for scientific accuracy and content remains entirely with the authors.

1 Fuchsberger FF, Kim D, Baranova N, Vrban H, Kagelmacher M, Wawrzinek R, Rademacher C. *eLife*, 2023, 12: e69415
2 Ohtsubo K, Marth JD. *Cell*, 2006, 126: 855–867
3 Kailemia MJ, Park D, Lebrilla CB. *Anal Bioanal Chem*, 2017, 409: 395–410
4 Pinho SS, Reis CA. *Nat Rev Cancer*, 2015, 15: 540–555
5 Rudd PM, Elliott T, Cresswell P, Wilson IA, Dwek RA. *Science*, 2001, 291: 2370–2376
6 Lowe JB. *Cell*, 2001, 104: 809–812
7 Pandey VK, Sharma R, Prajapati GK, Mohanta TK, Mishra AK. *Mol Biol Rep*, 2022, 49: 8109–8120
8 Costa AF, Campos D, Reis CA, Gomes C. *Trends Cancer*, 2020, 6: 757–766
9 Dwek RA, Butters TD, Platt FM, Zitzmann N. *Nat Rev Drug Discov*, 2002, 1: 65–75
10 Xu XD, Cheng H, Chen WH, Cheng SX, Zhuo RX, Zhang XZ. *Sci Rep*, 2013, 3: 2679
11 Chen Y, Ding L, Ju H. *Acc Chem Res*, 2018, 51: 890–899
12 Tommasone S, Allabush F, Tagger YK, Norman J, Köpf M, Tucker JHR, Mendes PM. *Chem Soc Rev*, 2019, 48: 5488–5505
13 Wu X, Delbianco M, Anggara K, Michnowicz T, Pardo-Vargas A, Bharate P, Sen S, Pristl M, Rauschenbach S, Schlickum U, Abb S, Seeberger PH, Kern K. *Nature*, 2020, 582: 375–378
14 Letschert S, Göhler A, Franke C, Bertleff-Zieschang N, Memmel E, Doose S, Seibel J, Sauer M. *Angew Chem Int Ed*, 2014, 53: 10921–10924
15 Laughlin ST, Baskin JM, Amacher SL, Bertozzi CR. *Science*, 2008, 320: 664–667
16 Wu ZL, Person AD, Zou Y, Burton AJ, Singh R, Burroughs B, Fryxell D, Tatge TJ, Manning T, Wu G, Swift KAD, Kalabokis V. *Glycobiology*, 2020, 30: 454–462
17 Ruhaak LR, Miyamoto S, Lebrilla CB. *Mol Cell Proteomics*, 2013, 12: 846–855
18 Saxon E, Luchansky SJ, Hang HC, Yu C, Lee SC, Bertozzi CR. *J Am Chem Soc*, 2002, 124: 14893–14902
19 Yang W, Nan H, Xu Z, Huang Z, Chen S, Li J, Li J, Yang H. *Anal Chem*, 2021, 93: 12265–12272
20 Liu H, Li X, Ren Y, Yang Y, Chen Y, Ju H. *J Am Chem Soc*, 2024, 146: 8780–8786
21 Shao Z, Yuan H, Zhou Z, Wang Y, Hou P, Nan H, Wang W, Tan W, Li J. *Angew Chem Int Ed*, 2022, 61: e202210069
22 Kang S, Zhu L, Wang W, Lu Y, You Z, Zhang C, Xu Y, Yang C, Song Y. *Sci China Chem*, 2022, 65: 1204–1211
23 Chen L, Lyu Y, Zhang X, Zheng L, Li Q, Ding D, Chen F, Liu Y, Li W, Zhang Y, Huang Q, Wang Z, Xie T, Zhang Q, Sima Y, Li K, Xu S, Ren T, Xiong M, Wu Y, Song J, Yuan L, Yang H, Zhang XB, Tan W. *Sci China Chem*, 2023, 66: 1336–1383
24 Zhang C, Zhou Z, Fu S, Yu C, Irfan M, Su X. *Nano Today*, 2023, 51: 101893
25 Wen X, Yuan B, Zhang J, Meng X, Guo Q, Li L, Li Z, Jiang H, Wang K. *Chem Commun*, 2019, 55: 6114–6117
26 Zhang X, Li R, Chen Y, Zhang S, Wang W, Li F. *Chem Sci*, 2016, 7: 6182–6189
27 Li J, Liu S, Sun L, Li W, Zhang SY, Yang S, Li J, Yang HH. *J Am Chem Soc*, 2018, 140: 16589–16595
28 Xu W, Hu F, Li J, Shang J, Liu X, Zeng Y, Wu Q, Wang F. *Sci China Chem*, 2023, 66: 3105–3115
29 Kobayashi H, Choyke PL. *Acc Chem Res*, 2011, 44: 83–90
30 Jia HR, Zhu YX, Duan QY, Wu FG. *Chem Soc Rev*, 2021, 50: 6240–6277
31 Peveler WJ, Algar WR. *ACS Chem Biol*, 2018, 13: 1752–1766
32 Fu Y, Qian H, Zhou X, Wu Y, Song L, Chen K, Bai D, Yang Y, Li J, Xie G. *Anal Bioanal Chem*, 2021, 413: 6929–6939
33 Xu L, Duan J, Chen J, Ding S, Cheng W. *Anal Chim Acta*, 2021, 1148: 238187
34 Xu L, Lu S, Wang H, Xu H, Ye BC. *Anal Chem*, 2023, 95: 15745–15754
35 Tao S, Han X, Shi D, Yu T, Long Y, Zou S, Lu S, Song L, Liu G. *Anal Chem*, 2024, 96: acs.analchem.4c02070
36 Xie T, Deng Y, Zhang J, Zhang Z, Hu Z, Wu T. *Nucleic Acids Res*, 2022, 50: 8431–8440
37 Zhang C, Wang Z, Liu Y, Yang J, Zhang X, Li Y, Pan L, Ke Y, Yan H. *J Am Chem Soc*, 2019, 141: 17189–17197
38 Humphrey W, Dalke A, Schulten K. *J Mol Graphics*, 1996, 14: 33–38
39 Shi Z, Castro CE, Arya G. *ACS Nano*, 2017, 11: 4617–4630
40 Makino K, Susaki EA, Endo M, Asanuma H, Kashida H. *J Am Chem Soc*, 2022, 144: 1572–1579
41 Dehnert KW, Baskin JM, Laughlin ST, Beahm BJ, Naidu NN, Amacher SL, Bertozzi CR. *ChemBioChem*, 2012, 13: 353–357
42 Prescher JA, Dube DH, Bertozzi CR. *Nature*, 2004, 430: 873–877
43 Caldwell RM, Flynn RA. *Israel J Chem*, 2023, 63: e202200059
44 Jonkman J, Brown CM. *J Biomol Tech*, 2015, 26: 54–65
45 Yoon D, Moon JH, Cho A, Boo H, Cha JS, Lee Y, Yoo J. *Molecules Cells*, 2023, 46: 337–344
46 Xiao H, Smeekens JM, Wu R. *Analyst*, 2016, 141: 3737–3745
47 Yoo J, Mashalidis EH, Kuk ACY, Yamamoto K, Kaeser B, Ichikawa S, Lee SY. *Nat Struct Mol Biol*, 2018, 25: 217–224